UNIVERSITÀ DEGLI STUDI DI PADOVA

Dipartimento di Fisica e Astronomia "Galileo Galilei"

Corso di Laurea in Fisica

Tesi di Laurea

Hamiltonian Lattice QED:

Propagating Waves in Empty Space

Propagazione Hamiltoniana di Onde in Elettrodinamica Quantistica su Reticolo

Relatore

Prof. Simone Montangero

Correlatore

Dr. Pietro Silvi

Laureando

Giacomo Guarda

Anno Accademico 2021/2022

Abstract

The propagation of waves in Hamiltonian Lattice Quantum Electrodynamics using a fully quantum many-body approach is a rather demanding theoretical problem. Even for the pure theory (under infinite electron mass), obtaining analytical solutions is extremely difficult without making some approximations. In this thesis, we consider a quantum link model with an electric energy-density cutoff on a ladder geometry. For simplicity, we choose small-dimensional representations for the gauge fields that still allow the spatial propagation of excitations. We then translate our QED problem to a quantum spin model that we can solve through exact diagonalization for small system sizes. In this theoretical framework, we focus our research on the ground state and on the dispersion relation, the Bloch States, and the Wannier Functions of the lowest energy band. These states can be seen as quasi-particle excitations at low energies, which represent the propagating waves that we aim to understand. We also look at the evolution of the system in real time under the influence of a localized time-dependent Hamiltonian which induces propagating waves.

Keywords:Propagating Waves, QED, Hamiltonian Lattice

Contents

Chapter 1

Introduction

Quantum electrodynamics (QED) has been historically described with a perturbative formulation as the value of the coupling ($\alpha \approx 1/137$) is small. This formulation allows for semi-analytical calculations by means of Feynman diagrams. However, the approach must be changed when the non-perturbative effects become relevant, as is the case - for example - with Quantum Chromo-Dynamics. One of the main non-perturbative approaches is via lattice regularization through Lattice Gauge Theories (LGTs). LGTs were first introduced by Wilson [15] in their Lagrangian formulation, which is an ideal setup for Monte Carlo Simulations [4, 11, 5, 6]. The continuum limit in Wilson's LGTs is retrieved by taking to zero the limit for the lattice spacing. Later Kogut and Susskind introduced an alternative formulation [9, 8] called Hamiltonian Lattice Field Theory, which is the basis for our theoretical framework.
The Hamiltonian formulation of LGTs discretizes the spatial dimensions, whereas the time dimension remains real and continuous. In the general 3-dimensional case the system is described by lattice sites connected by links. These links are referred to by the position of the lattice site ($\vec{r}$) and the direction of the link itself ($\hat{m}_d$). For example, given a spatial cubic lattice of lattice spacing a, a link is referred to as $(\vec{r} = r_x a\hat{x} + r_y a\hat{y} + r_z a\hat{z}, \hat{m}_d) = ((r_x, r_y, r_z), \hat{m}_d)$ with $r_i \in \mathbb{Z}$ and $d = x, -x, y, -y, z, -z$ with the convention $\hat{m}_{-d} = -\hat{m}_d$ (see Fig.1.1).

This description gives rise to an interacting quantum lattice, or - in other words - a quantum many-body system. Its configuration space grows exponentially, thus making the system very difficult to analyze as its size grows. Let us consider a system with N_d sites and N_l links, each independent from the rest of the system. If each link has l possible states and each site has d possible states, the number of resulting configurations is $M_C = d^{N_d} \cdot l^{N_l}$. Ideally, we want to retrieve the "infinite-space" limit normally used to study the propagation of electromagnetic waves. To do this we would need to take to infinity the limit for N_d, N_l.

Figure 1.1: Spatial cubic lattice site with nearest links

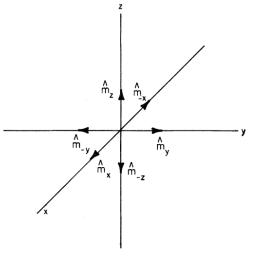

We restrict our study to a 2-dimensional ladder geometry (square lattice of 2xN sites, see Fig.1.2) to further simplify the problem. This condition translates into the following restrictions:

$$r_z = 0 \tag{1.1}$$
$$r_y = 0, 1 \tag{1.2}$$
$$r_x = 0, 1, ..., N-1 \tag{1.3}$$

$$d = \begin{cases} x, -x, y \ \textit{if} \ r_y = 0 \\ x, -x, -y \ \textit{if} \ r_y = 1 \end{cases} \tag{1.4}$$

where N is what we call the "system size"
We also simplify the notation used to identify the links by ignoring r_z: $(r_x, r_y, 0) \equiv (r_x, r_y)$.

Upon this theoretical basis, we then introduce a Gauge Theory. A Gauge Theory is defined by the promotion of a global symmetry to a local one. For Quantum Electrodynamics (QED) the global symmetry is the conservation of charge[1]. This symmetry imposes a constraint that is to be satisfied at every point in space, or - in our case - at each lattice site.

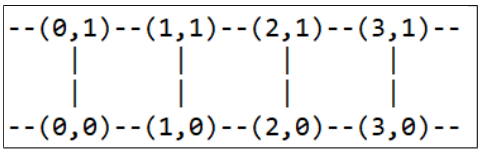

Figure 1.2: Nomenclature of the sites of the square 2xN lattice

$$\int_{all\ space} \rho(\vec{x}) d^3x \equiv \text{cost} \tag{1.5}$$

$$\Longrightarrow \vec{\nabla} \cdot \vec{E}(\vec{x}) = \rho(\vec{x}) \tag{1.6}$$

$$\Longrightarrow \sum_{d=x,y,z} (E_{(\vec{r},-\hat{m}_d)} - E_{(\vec{r},\hat{m}_d)}) = q(\vec{r}) \tag{1.7}$$

where $q(\vec{r})$ measures the electric charge at the site $\vec{r}$.
This local constraint considerably reduces the number of possible configurations, thus enabling us to study systems of greater size than it would have been otherwise possible. However, the growth of the number of configurations is still exponential.
In this description, the fermionic matter field lives in the lattice sites while the bosonic gauge field lives in the links. All charged particles enter QED theory. Among these particles, electrons and positrons have the most impactful contribution to the model as they are the lightest. For our purposes, we take into consideration a system with no particles at $t = 0$. We also take the infinite-mass limit for the fermions in order to ignore the vacuum fluctuations that would otherwise generate particle-antiparticle pairs. Under these hypotheses, we can then ignore the fermionic matter field, which will be equal to zero at all times. The Hamiltonian operator ($\hat{H}$) and the particle-number operator ($\hat{N}$) commute ($[\hat{H}, \hat{N}] = 0$). We can then diagonalize them simultaneously and restrict ourselves to the eigenspace of $\hat{N}$ with eigenvalue $n = 0$.
To formalize these concepts we must now choose a mathematical description for our system. In the standard formulation of Wilson's Lattice Gauge Theories an element (which is an operator) of a Gauge Group is introduced at each link. The operator usually spans an infinite-dimensional Hilbert Space: this reflects the fact that the intensities of the electric field at each link are not bound. For the purposes of this study, we use exact diagonalization methods. The infinite dimension would therefore make the problem difficult to solve with this technique. We thus adopt a quantum link model [7, 13, 3] formulation: the operators at each link are finite-dimensional and can be described by spin variables in a chosen representation (for example $S = 1/2$ or $S = 1$). This description corresponds to an energy-density cutoff and will be an accurate approximation for the system only at low energies. The quantum link formulation keeps gauge invariance intact as Wilson's LGTs. However, for quantum link models the continuum limit is obtained by a mechanism called "dimensional reduction" [14, 1] and not through vanishing lattice spacing.
We now have a quantum spin model, which is much simpler to analyze compared to the starting description. The lowest spin representation which still allows propagating waves is $S = \frac{1}{2}$ on the horizontal links and $S = 1$ on the vertical links (we will reference these values as $(\frac{1}{2}, 1)_S$). Ideally, we would like to take to infinity the limit for S, which corresponds to no energy-density cutoff.
We also need to translate the original electromagnetic equilibrium Hamiltonian (H) to a spin Hamiltonian ($\hat{H}$) that acts on the links. The classical Hamiltonian is:

$$H = \frac{1}{2} \int_{all\ space} (E^2 + B^2) d^3x \tag{1.8}$$

We use the following spin Hamiltonian:

[1] A constraint on the system can be thought of as a symmetry

$$\hat{H} = \hat{H}_E + \hat{H}_B \tag{1.9}$$

$$\hat{H}_E = g^2 \sum_{links} \hat{S}_z^2 \tag{1.10}$$

$$\hat{H}_B = \frac{1}{g^2} \sum_{plaquettes} \hat{H}_{B,p} \tag{1.11}$$

$$\hat{H}_{B,p} = \hat{H}^+_{B,p} + \hat{H}^-_{B,p} \tag{1.12}$$

$$\hat{H}^+_{B,p} = \hat{S}^+_{((r_x,0),\hat{m}_x)} \otimes \hat{S}^+_{((r_x+1,0),\hat{m}_y)} \otimes \hat{S}^-_{((r_x+1,1),-\hat{m}_x)} \otimes \hat{S}^-_{((r_x,1),-\hat{m}_y)} \tag{1.13}$$

$$\hat{H}^-_{B,p} = (\hat{H}^+_{B,p})^* \tag{1.14}$$

where g is the coupling and $\hat{S}_z, \hat{S}^+, \hat{S}^-$ are the normal spin operators
We must bear in mind that $\hat{H}_B$ as defined here has negative and positive energy eigenvalues, unlike its classical counterpart $H_B \propto B^2$. However, this is not an issue since Hamiltonians are defined up to constants. This Hamiltonian would be sufficient for the analysis of the equilibrium, but since we are interested in the propagation of waves we also need to construct a Hamiltonian $\hat{H}_A$ that perturbs said equilibrium. We consider a simple model for a localized emitter of excitations that is able to induce the propagation of waves. This Hamiltonian $\hat{H}_A$ is time-dependent and acts on the opening links of a system with open-boundary conditions [2].

[2]Boundary conditions will be explained in the next chapter

Chapter 2

Methods

The analysis of the system consists of multiple steps: we first find the possible configurations and we then construct the relevant operators. Finally, we analyze the operators to extract the relevant information.

2.1 Constructing the Configurations

First of all, we need to identify the possible configurations of our system. In order to do this, we translate the local Gauge invariance in terms of operators acting on the spin variables:

$$\begin{cases} \hat{E}_{((r_x,r_y),-\hat{m}_x)} - \hat{E}_{((r_x,r_y),+\hat{m}_x)} - \hat{E}_{((r_x,r_y),\hat{m}_y)} = 0 \ \textit{if} \ r_y = 0 \\ \hat{E}_{((r_x,r_y),-\hat{m}_x)} - \hat{E}_{((r_x,r_y),+\hat{m}_x)} + \hat{E}_{((r_x,r_y),-\hat{m}_y)} = 0 \ \textit{if} \ r_y = 1 \end{cases} \tag{2.1}$$

$$\textit{with} \ \hat{E}_{((r_x,r_y),\hat{m}_d)} \equiv \hat{S}_{z,((r_x,r_y),\hat{m}_d)} \tag{2.2}$$

The configurations we show in the pictures throughout this paper are all eigenstates $|s\rangle$ of eigenvalue s of the $\hat{S}_z$ operator for each link. To graphically represent the eigenstate of a link we use arrows: the direction of the arrows represents the sign of s while the number of arrows represents the absolute value of s (see Fig.2.1(a)). Each arrow stands for half a quantum of the electric field. For example if we choose $S = \frac{1}{2}$, the eigenvalue $s = +1/2$ is represented by one arrow. If we choose $S = 1$ the eigenvalue $s = +1$ is represented by two arrows.

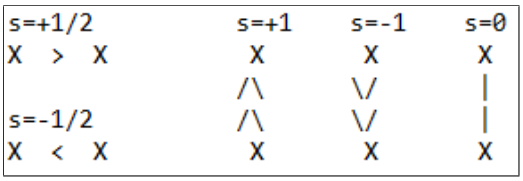

(a)

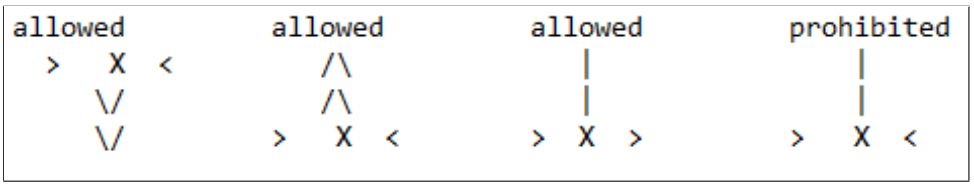

(b)

Figure 2.1: Explanation of the graphical notation of the configuration drawings, together with some examples of local configurations allowed by Gauss' Law
(a) shows the relation between the arrows and the eigenvalue of $\hat{S}_z$ on the link
(b) shows some examples of allowed local configurations

We also need to define the boundary conditions for the configuration. In the equilibrium analysis we choose periodic boundary conditions (PBCs): for a system of size N the $\hat{m}_x$ links of the $(N-1, r_y)$ site are the $-\hat{m}_x$ links of the $(0, r_y)$ site. PBCs allow us to reconstruct the dispersion relation by decoupling Bloch k-wavevector subspaces. On the contrary, for the out-of-equilibrium (OOE) dynamics we choose open boundary conditions (OBCs), as we aim to introduce a localized antenna that would break the translational symmetry anyway. Therefore, in the OOE case there are no restrictions on the $-\hat{m}_x$ links of the $(0, r_y)$ site or on the $\hat{m}_x$ links of the $(N-1, r_y)$ site.
We then construct the allowed configurations at a given system size with these restrictions in mind. First, we find all the possible super-plaquettes (SPs) at the chosen spin representation. An SP is constituted by the four lattice sites and the four links of a single plaquette together with the four adjacent horizontal links (see Fig.2.2(a)). We then find which subset of all possible SPs can follow each SP while maintaining the gauge invariance intact.

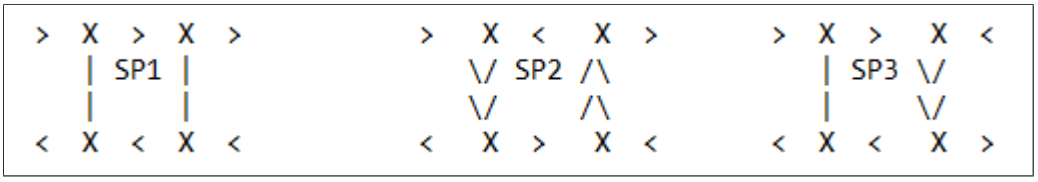

(a)

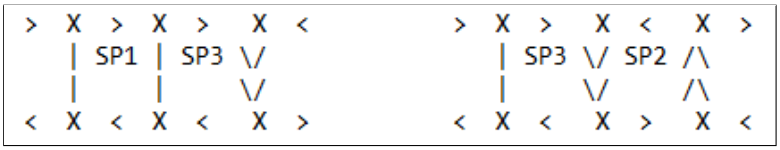

(b)

Figure 2.2: Construction of SP sequences.
(a) shows some examples of allowed SPs at $(\frac{1}{2}, 1)_S$
(b) shows that SP3 can follow SP1 but not SP2, while SP2 can follow SP3 but not SP1

The size N is defined by the number of vertical links. Therefore, for a system of size N with open boundary conditions (OBCs), the possible configurations are all possible sequences of $N-1$ SPs: the starting SP has two vertical links and every other SP adds one link. Alternatively, if the boundary conditions are periodic we also check that the "closing SP" is among the allowed SPs, or - in other words - that the $\hat{m}_x$ links of the $(N-1, r_y)$ sites have the same values as the $-\hat{m}_x$ links of the $(0, r_y)$ sites. For example, in Fig.2.2(b) the sequence on the right satisfies PBCs, while the sequence on the left does not. Each SP is identified by a number (for example $\overline{1}, \overline{2}, \ldots, \overline{10}, \ldots$), and each configuration is identified by the sequence of the numbers which identify the SPs composing it (for example $|\overline{1}\ \overline{11}\ \overline{4}\rangle$). The number of configurations (M_C) grows exponentially with the system size.

It is difficult to find an analytic formula for the number of configurations, but for the lowest spin representation $(\frac{1}{2}, 1)_S$ it is doable. There are 10 possible SPs for this spin representation. Two of these SPs can only be followed by the same SP, e.g. SP1 can be followed only by SP1, thus creating two distinct configurations. The other 8 SPs can each be followed by 2 other SPs among said 8, thus creating $M = 8 * 2^{(N-3)}$ configurations: there are 8 possibilities for the first SP while the $(N-1)th$ SP is determined uniquely by the PBCs. The analytic formula is then:

$$M_C(N) = 2^N + 2 \tag{2.3}$$

For other spin representations, for example $(1, 1)_S$, the exponential growth is confirmed by the exponential fit. As the spin representation grows, so does the base of the exponential. This is to be expected, since the number of possible SPs also grows.

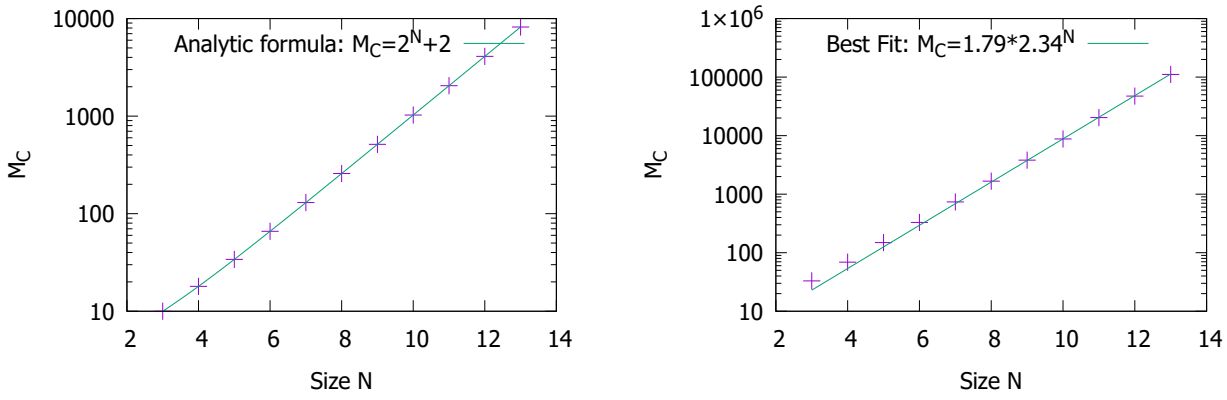

(a) (b)

Figure 2.3: M_C for systems of different sizes with PBCs.
The graph (a) refers to $(\frac{1}{2}, 1)_S$, while the graph (b) refers to $(1, 1)_S$

2.2 Constructing the Operators

In order to study the equilibrium of the system, we are interested in the equilibrium Hamiltonian ($\hat{H}$), the translational operator ($\hat{T}$), and the inversion operator ($\hat{I}$). We find the matrix elements of the operators by studying how they act on each configuration.
To construct $\hat{T}$ for each configuration we shift the sequence of SPs periodically (for example $\hat{T}|\overline{1}\ \overline{2}\ \overline{3}\rangle = |\overline{3}\ \overline{1}\ \overline{2}\rangle$) and find the configuration corresponding to the shifted sequence. The translational matrix is unitary and given the PBCs and the integer size of the system the eigenvalues T_{v_k} of the matrix are known beforehand:

$$T_{v_k} = \begin{cases} e^{ik} \ with\ k = \frac{-(N-1)+2j}{2N} 2\pi, j = 0, ..., N-1 & for\ N\ odd \\ e^{ik} \ with\ k = \frac{-N+2j}{2N} 2\pi, j = 0, ..., N-1 & for\ N\ even \end{cases} \tag{2.4}$$

To construct $\hat{I}$ we invert the sequence of SPs for each configuration and then substitute every SP with its horizontal reflection. We then find the configuration corresponding to this new sequence.
Constructing the Hamiltonian matrix is more complicated. This difficulty is caused by the fact that our configurations are eigenstates of $\hat{H}_E$ but not of $\hat{H}_B$. The electric part of the $\hat{H}$ is then a diagonal matrix with the diagonal value corresponding to each configuration equal to the eigenvalue of the operator itself for the given configuration. To find the matrix elements of the magnetic part we first find its effect on every SP. Calling $|s\rangle$ the $\hat{S}_z$ eigenstate of a link with spin representation S, the effect of $\hat{S}^+$ and $\hat{S}^-$ are the following:

$$\langle s'|\hat{S}^+|s\rangle = \delta_{s',s+1}\sqrt{S(S+1) - s' \cdot s} \tag{2.5}$$

$$\langle s'|\hat{S}^-|s\rangle = \delta_{s'+1,s}\sqrt{S(S+1) - s' \cdot s} \tag{2.6}$$

Therefore, the magnetic plaquette operator (see Eq.(1.12)) has different effects on different SPs as can be seen in Fig.2.4. For every SP we can have three mutually exclusive cases:

- the magnetic plaquette operator transforms the SP into two different not-allowed SPs
- the magnetic plaquette operator transforms the SP into one allowed SP and one not-allowed SP
- the magnetic plaquette operator transforms the SP into two different allowed SPs

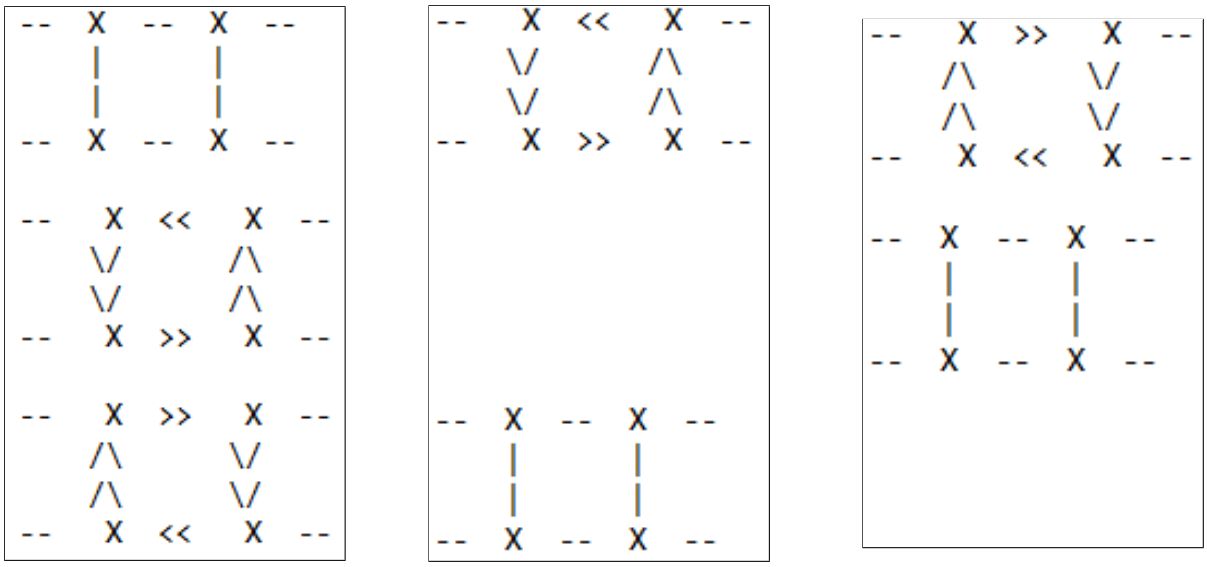

Figure 2.4: The first row represents the starting SP, the second row represents the effect of $\hat{H}^{+}_{B,p}$(see Eq.(1.13)) while the third row represents the effect $\hat{H}^{-}_{B,p}$(see Eq.(1.14),Eq.(1.13)). If the row is empty it means that the operator transforms the SP into a not-allowed SP. Only the resulting eigenstate is shown while the numeric part of the result is omitted.

After analyzing the effect on the SPs, we take every configuration in turn and make the operator act on each of its SPs (including the closing plaquette, formed by the last and the first vertical links). We then check if the resulting configurations are allowed and, if that's the case, we add the relative matrix elements (the numerical values the ones in Eq.(2.5),Eq.(2.6)) to the Hamiltonian matrix. The resulting Hamiltonian matrix is Hermitian as we expect. The Hamiltonian matrix is slightly different in the OOE case since there is no closing plaquette.
In order to study the OOE case, we also need to construct $\hat{H}_A$. This operator acts on the first SP and has the following expression:

$$\hat{H}_A = \Omega(t) \cdot \left(e^{i\theta} \hat{S}^{+}_{((0,0),-\hat{m}_x)} \otimes \hat{S}^{+}_{((0,0),\hat{m}_y)} \otimes \hat{S}^{-}_{((0,1),-\hat{m}_x)} + H.c. \right) \tag{2.7}$$

where $\Omega(t)$ is a function of time.
To construct its matrix we proceed similarly to the Hamiltonian case, namely we analyze the effect of the operator on each configuration.

2.3 Analysis of the System

In the equilibrium case, we simultaneously diagonalize the Hamiltonian matrix and the Translational matrix in order to study the dispersion relation and the low energy eigenstates, whereas in the OOE case we analyze the time evolution of the Ground State (GS) under the effect of $\hat{H}_A$.

2.3.1 Analysis of the Equilibrium

To simultaneously diagonalize $\hat{T}$ and $\hat{H}$, we exploit our knowledge of the translational eigenvalues T_{v_k}. We first find the kers of $(\hat{T} - T_{v_k}\hat{\mathbb{I}})$ for every k, thus finding the eigenspaces of the translational eigenvalues. We then use this information to change the base of our Hamiltonian matrix thus breaking $\hat{H}$ into blocks. After that, we find the eigenstates and eigenvalues of $\hat{H}$ for the single blocks. Lastly, we change the simultaneous eigenstates to the original base. If we are only interested in the low-energy eigenstates, we can exploit a dedicated algorithm of the "scipy" Python package able to find the first closest eigenstates to a certain target value.
These states are the Bloch states Ψ_{nk} of our system: k identifies the translational eigenvalue and n identifies the energy band and, therefore, the energy eigenvalue. Among these states, we also find the

GS of our system. After that, we try to obtain localized functions through the method of the Wannier Functions (WFs) Φ_j. The simplest method to calculate the WFs of the n band is the following:

$$\Phi_j = \frac{1}{\sqrt{N}} \sum_k e^{-ikj} \Psi_{nk} \tag{2.8}$$

In order to give an intuitive idea of the form of the WFs, we define a local operator which captures the intensity of the electric field proximate to the r_x-esime vertical link (identified by $((r_x, 0), \hat{m}_y)$ or $((r_x, 1), -\hat{m}_y)$), which we will call "electric energy density operator":

$$\mathcal{E}_{r_x} = \frac{1}{2}\left(\hat{S}^2_{z,((r_x,0),-\widehat{m_x})} + \hat{S}^2_{z,((r_x,1),-\hat{m}_x)}\right) + \hat{S}^2_{z,((r_x,0),\hat{m}_y)} + \frac{1}{2}\left(\hat{S}^2_{z,((r_x,0),\hat{m}_x)} + \hat{S}^2_{z,((r_x,1),\hat{m}_x)}\right) \tag{2.9}$$

Since it can be proven that changing the value of j of the WF results in a spatial translation of the function itself only the WFs for $j = 0$ will be represented.

2.3.2 Analysis of the Out of Equilibrium Dynamics

To study the propagation of the waves we first prepare the system in its ground state and then study its evolution in time under the effect of $\hat{H}_T(t) = \hat{H} + \hat{H}_A(t)$. To prepare the system in the GS we first diagonalize the Hamiltonian matrix (while imposing $\hat{H}_A = 0$) and find the lowest energy eigenstate. In the $(\frac{1}{2}, 1)_S$ case, the OBCs induce a degeneracy in the GS. There are two states which share the lowest energy eigenvalue while differing only because of vertical reflection, as can be seen in Fig.2.5.

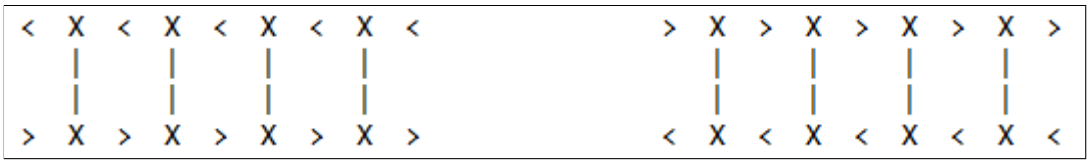

Figure 2.5: One of the two lowest energy eigenstates contains the configuration on the right with associated probability p_0 while the other contains the configuration on the left with the same probability p_0

For the purposes of our study, we select the $(1, 1)_S$ representation, which does not suffer from any degeneracy and thus has a unique GS.
After having found the GS we make it evolve through the action of $\hat{H}_A$. The time-dependent part of this matrix is the $\Omega(t)$ function, which is related to the strength and the speed of the induced excitation. The evolution of the system is then:

$$|\psi(t)\rangle = e^{-i\hat{H}_T(t)t}|\psi(0)\rangle \tag{2.10}$$

$$i\hbar\frac{d|\psi(t)\rangle}{dt} = \hat{H}_T(t)|\psi(t)\rangle \tag{2.11}$$

To simplify the calculations we choose $\hbar = 1$. We can then solve the linear differential equation with the Runge-Kutta numerical integration method at fourth order (RK4) [2, 12]. In the following equations v_{in} is the GS initial vector, h is the timestep, L is the number of configurations and we let

$\hat{H}_T$ equal H.

$$\frac{dv_i(t)}{dt} = \sum_{j=1}^{L} -iH_{ij}(t)v_j(t) \tag{2.12}$$

$$v_{i,0} = v_{in,i} \tag{2.13}$$

$$v_{i,n+1} = v_{i,n} + \frac{1}{6}(k_1 + 3k_2 + 2k_3 + k_4)h \tag{2.14}$$

$$k_1 = -iH_{ij}(nh)v_{j,n} \tag{2.15}$$

$$k_2 = -iH_{ij}(nh + \frac{h}{2})(v_{j,n} + \frac{h}{2}k_1) \tag{2.16}$$

$$k_3 = -iH_{ij}(nh + \frac{h}{2})(v_{j,n} + \frac{h}{2}k_2) \tag{2.17}$$

$$k_4 = -iH_{ij}(nh + h)(v_{j,n} + hk_3) \tag{2.18}$$

The success of this method revolves around finding an appropriate time step to make the algorithm converge. In order to find a good time step, we need to consider which energy levels we want to access. We then find the maximum energy difference between these levels and then construct an appropriate time scale. A good starting point is the time scale derived from the dispersion relation. For example, if the GS energy is $H_{GS} = -3$ and we want to induce an excitation in the $n = 1$ band with a maximum energy of $H_{max} = 7$, the associated time scale[1] is:

$$t_s = \frac{\hbar}{H_{max} - H_{GS}} = \frac{1}{H_{max} - H_{GS}} = 0.1 \tag{2.19}$$

From this starting point, we can then try - for example - a time-step of $h = \frac{1}{10}t_s$ or smaller, and see if there are any measurable differences under changes of the time step h. These differences could indicate the convergence or non-convergence of the algorithm. To measure these differences we look at the distances between the vectors at a certain time point obtained with different time steps. We define the distance as:

$$d(|v_1\rangle, |v_2\rangle) = \sqrt{1 - \frac{|\langle v_1|v_2\rangle|^2}{||v_1||^2||v_2||^2}} \tag{2.20}$$

We finally check if the wave propagation velocity obtained from the OOE analysis is consistent with the velocity obtained from the dispersion relation. To study the wave propagation we utilize the "electric energy density" $\mathcal{E}$ defined in Eq.(2.9) and we also construct a "magnetic density operator" defined as:

$$\mathcal{B}_{r_x} = (\hat{S}^{+}_{((r_x,0),\hat{m}_x)} \otimes \hat{S}^{+}_{((r_x+1,0),\hat{m}_y)} \otimes \hat{S}^{-}_{((r_x+1,1),-\hat{m}_x)} \otimes \hat{S}^{-}_{((r_x,1),-\hat{m}_y)} + H.c. \tag{2.21}$$

We can then use these energy density operators as a coarse indicator to measure the wave propagation velocity: we look at the peaks of the expectation values in the different lattice sites as time passes. This gives us a gross estimator of the Lieb-Robinson velocity [10] that we can then compare to the maximum group velocity ($\ddot{v}_g$) obtained from the analysis of the equilibrium:

$$\ddot{v}_g = max\frac{|E_j - E_i|}{|k_j - k_i|} \tag{2.22}$$

where (k_i, E_i) refer to the couple eigenvalues of a Bloch State in a given band, $|j - i| = 1$ and $\hbar = 1$.

[1] The values are for the sake of pure exemplification but do not correspond to any actual result

Chapter 3

Results

The main part of our research focuses on the analysis of the equilibrium of the system. This allows us to get an insight into the complex mechanisms at play. After this characterization, we look into the out-of-equilibrium dynamics through simple wave propagation.

3.1 Ground State

The GS is the starting point for the OOE dynamics. Therefore, we want to understand the composition of the GS for different spin representations and couplings. We show the results for $(1,1)_S$ as they are more visually intuitive compared to the $(\frac{1}{2},1)_S$ case. This analysis allows us to better understand the properties of the system itself, as it is possible to obtain a well-defined hierarchy of the types of configurations energy-wise.
As expected, the configuration probability is invariant under spatial translation, horizontal reflection, and vertical reflection, as shown in Fig. 3.1. In the graphs we then show the sum of all probabilities of configurations which only differ because of these transformations.

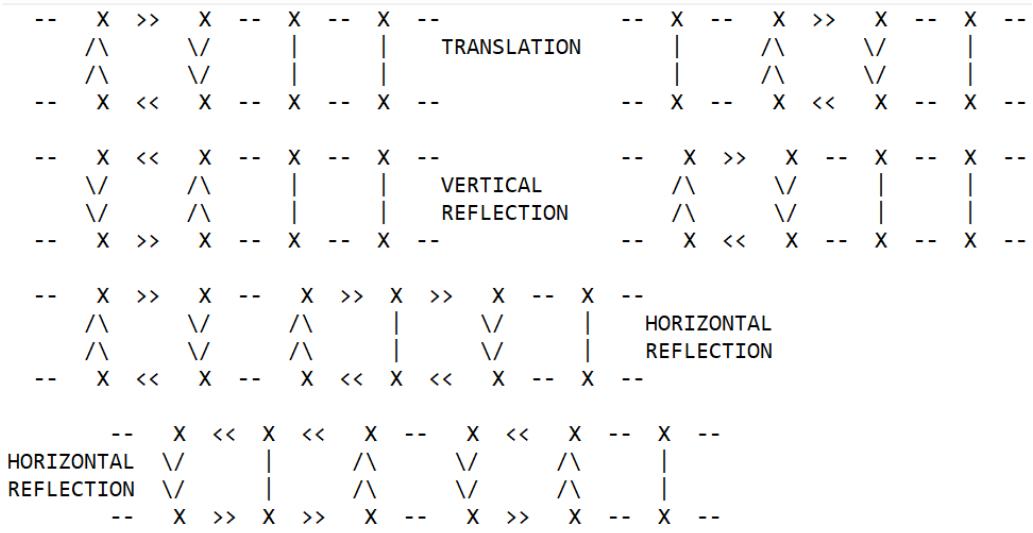

Figure 3.1: The probabilities of the configurations before the transformation are the same as the probabilities of the configurations after the transformation.

The main component of the GS is always the zero-excitation configuration. The probability associated with this configuration increases together with the coupling, (see Fig. 3.3(i)) ranging from about 0.04 at very low couplings ($g \approx 0.1$) to almost 1 at very high couplings ($g \approx 4$). This result is to be expected, as the coupling is a measure of the importance of the electric part $\hat{H}_E$ of the Hamiltonian

which measures the total electric field of a configuration. Therefore, high values of the coupling cause an increase in the energy cost of non-zero electric field values on the links.
In the strong coupling regime the electric part of the Hamiltonian rules the hierarchy, which is therefore well-defined. Different types of configurations, e.g. 2-plaquette excitations and 3-plaquette excitations (see Fig.3.2), do not mix in the probability hierarchy. On the contrary, this order gets broken down in a weak coupling regime.

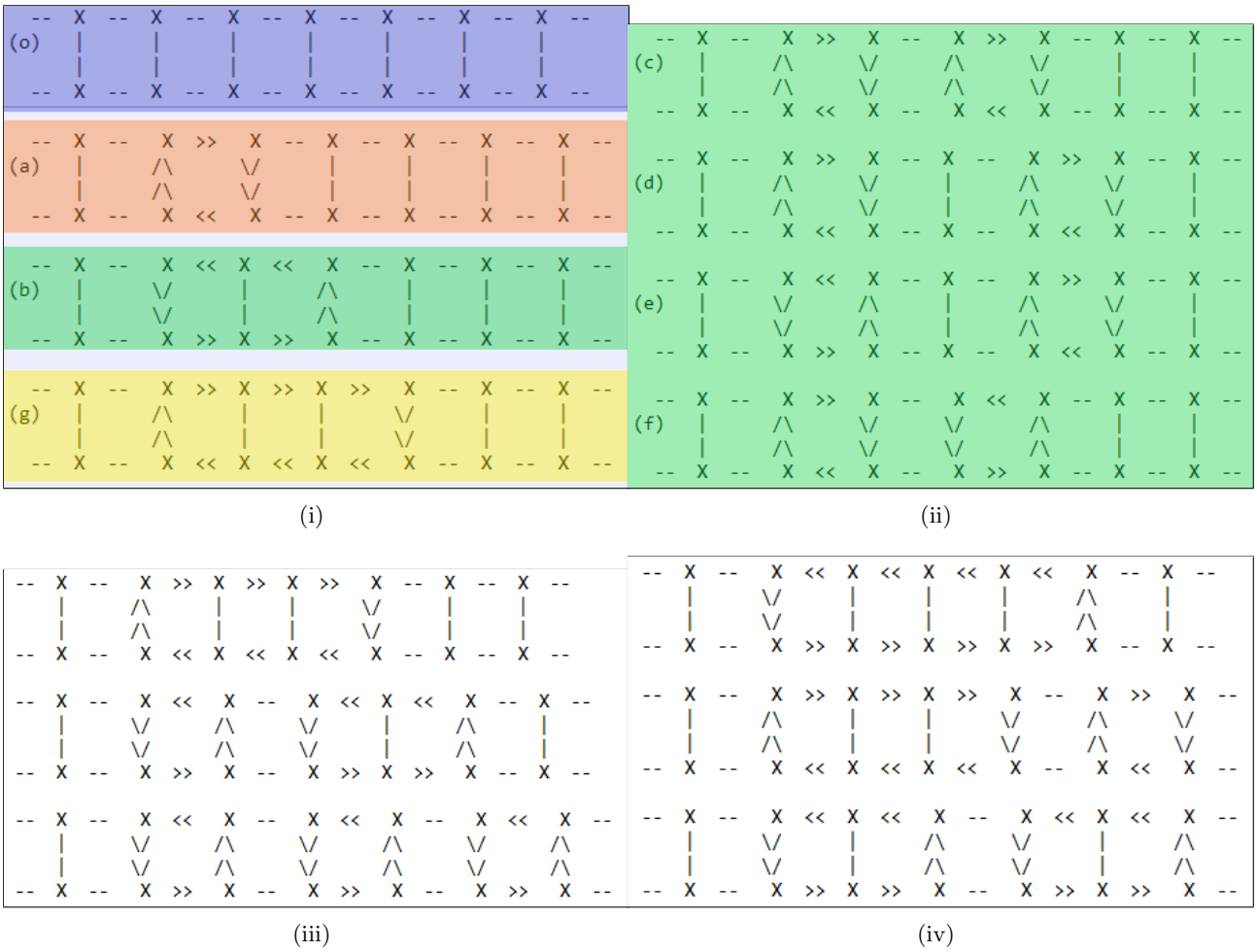

Figure 3.2: Every figure represents the configurations in descending probability order. The size is $N = 7$ while the spin representation is $(1, 1)_S$.
(i) shows the order induced by the number of excited plaquettes (only one configuration is shown for every "n-plaquette" type of excitation).
(ii) shows the order induced by $\hat{H}_B$.
(iii) and (iv) show the order induced by the fragmentation of the excitation.

First of all, we address the strong coupling regime. In this regime, the higher the number of excited plaquettes is, the lower the associated probability will be, as can be seen in Fig.3.2(i). This effect can be explained by the fact that the larger the excitation is, the higher the energy value associated with $\hat{H}_E$ will be. However, contrary to what one would guess when looking at the expression of $\hat{H}_E$, the determining factor is not the number of excited links, but the number of excited plaquettes.
If the number of excited plaquettes remains constant, the fragmentation of the excitation becomes the determining factor in the probability hierarchy. The higher the number of distinct loops is, the lower the associated probability is, as can be seen in Fig.3.2(iii). This can be explained by both the magnetic and electric parts of $\hat{H}$, as the fragmentation increases the number of excited links and therefore the energy associated with $\hat{H}_E$. Besides, the presence of more loops introduces a magnetic component in the determination of the associated energy. This magnetic component describes how the loops interact with each other. Moreover, the smaller the fragmented loops are, the higher the

associated probability is, as can be seen in Fig.3.2(iv).
The magnetic interaction can be explained by the way $\hat{H}_B$ can transform a configuration with separate loops. Two clockwise (or anticlockwise) loops can be connected into a single loop by $\hat{H}_B$: this effect gives a negative energy contribution to the configuration, thus increasing its probability. This "connection" is not possible if the loops of the configuration have opposite directions. Therefore, for these configurations the associated probability is lower. Moreover, the closest the loops are, the stronger the magnetic interaction will be. Therefore, if the interactions give a negative energy contribution, close-loops configurations are favored, whereas if the energy contribution is positive, distant-loops configurations are preferred. This is clearly seen in Fig.3.2(ii).
In the weak-coupling regime, the order induced by the magnetic interaction does not change. On the contrary, the order induced by the number of excited plaquettes and the fragmentation gets broken down. This effect is caused by the energy differences related to $\hat{H}_B$, which become dominant in this regime, and therefore supersede the order induced by $\hat{H}_E$.
We now delve a little deeper into the configuration probability for 1-plaquette and 2-plaquette configurations. The mixing effect produced by $\hat{H}_B$ in a weak coupling regime can be clearly seen in both graphs in Fig.3.3. At weak couplings, the magnetic effect is so strong that the negative-energy effect of $\hat{H}_B$ on two 1-plaquette loops configuration makes the total probability of 2-plaquette excitations higher than that of 1-plaquette excitations (see Fig.3.3(i)). Fig.3.3(ii) instead, shows how a 3-plaquette consecutive excitation configuration gets mixed in between two 1-plaquette loops configurations at weak couplings. Fig.3.3(ii) also shows that the magnetic order induced on two 1-plaquette loops configurations remains stable across a wide range of couplings, even after the mixing effects disappear.

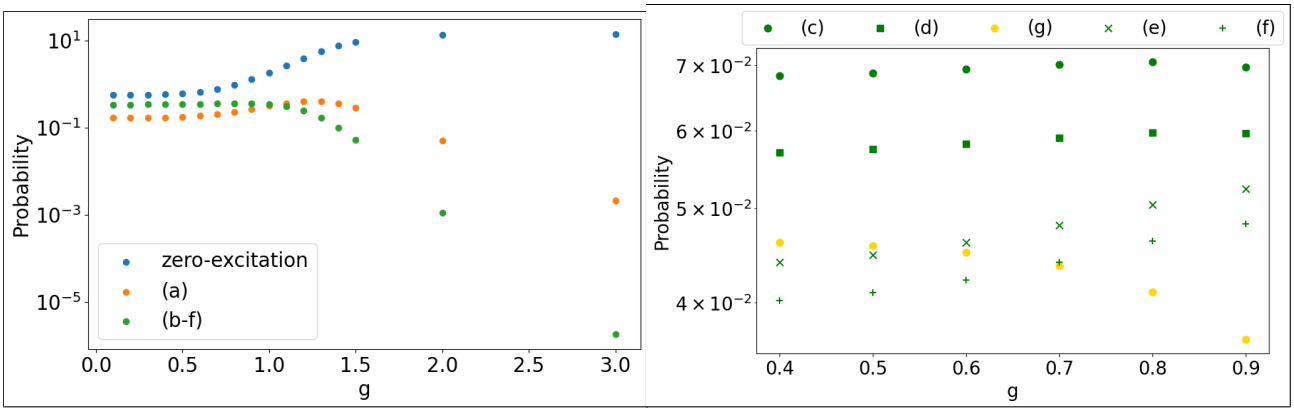

(i) (ii)

Figure 3.3: These graphs show the probability of different configuration types for $N = 7$ and $(1, 1)_S$. All letters refer to the configurations in Fig.3.2.
(i) shows the total probability for the zero-excitation configuration, the 1-plaquette excitation configurations and the 2-plaquette excitation configurations.
(ii) shows the probabilities of the different types of 2-plaquette non-consecutive excitations together with the probability of the consecutive 3-plaquette excitation

3.2 Energy Bands

In empty space, light travels at a constant velocity, and the dispersion relation is therefore linear. However, this is not what we have found in our study. This result is probably due to our approximations, namely the energy cut-off and the finite size of the system.
To study the dispersion relation, we look at the wave vector and at the energy simultaneous eigenvalues (k, H_v) found through the simultaneous diagonalization of $\hat{T}$ and $\hat{H}$ for different values of the coupling. The first thing to notice is the different behaviour at different spin representations $(\frac{1}{2}, 1)_S$ and $(1, 1)_S$, which can be seen in Fig. 3.4 and Fig.3.5.

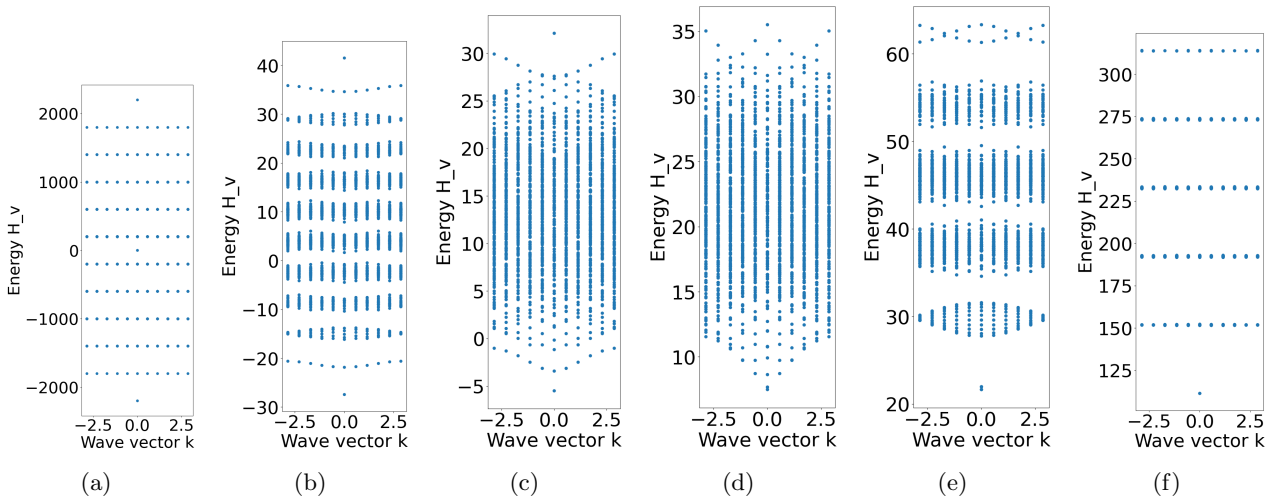

Figure 3.4: Every figure represents all the (k, H_v) couples at $N = 11$ and $(\frac{1}{2}, 1)_S$ for different values of the coupling: $g = 0.1$ (a), $g = 0.8$ (b), $g = 1.1$ (c), $g = 1.4$ (d), $g = 2$ (e) and $g = 4.5$ (f).

We first look at the $(\frac{1}{2}, 1)_S$ representation for $N = 11$. At very low couplings we observe 10 different flat energy bands, symmetric under inversion of the H_v sign, and there's also a distinct GS and a symmetric maximum energy state (see Fig.3.4(a)). All bands apart from the highest and lowest ones suffer from degeneracy. The low energy degenerate band (the band with $H_v \approx -15$ in Fig.3.4(b)) could be composed of the sums of two quasi-particle excitations, a quasi-particle excitation being an excitation of the lowest energy band. As the coupling grows the degeneracy of the central bands disappears (see Fig.3.4(b)) and for intermediate couplings these bands mix together (see Fig.3.4(c)–(d)). The lowest energy band curves but remains separate from the bulk until intermediate couplings ($g \approx 1.2$), after which it mixes disorderly with the other couples (see Fig.3.4(d)). The high energy band also curves, but mixes together with the other couples at lower values of the coupling in comparison to the lowest energy band (see Fig.3.4(c)).
As the coupling continues to grow, the degeneracy reappears (see Fig.3.4(e)), but the symmetry under H_v inversion does not. In this regime, the highest energy and the GS also suffer from degeneracy. At very high couplings the flatness of the bands reappears (see Fig.3.4(f)). The system thus seems to exhibit an insulating behaviour both at very high and very low couplings for $(\frac{1}{2}, 1)_S$. This system also has a clear low energy band from $g \approx 0$ until $g \approx 1.2$. We are particularly interested in this band since our approximation, namely the energy cutoff, holds well at low energies.
The behaviour of the dispersion relation can be explained through the electric and magnetic contributions of the Hamiltonian. At very low couplings $\hat{H}_E$ is nearly irrelevant and therefore the dispersion relation is determined by $\hat{H}_B$, which can give both positive and negative energy contributions depending on the interaction between the different excitations[1]. For intermediate couplings the contributions to the energy eigenvalue from the electric and magnetic terms have the same order of magnitude, thus removing the degeneracy. As the coupling continues to grow, $\hat{H}_E$ gives the first-order contribution to the energy eigenvalue, thus creating separate bands that share the same electric energy value. The degeneracy of the bands is removed by $\hat{H}_B$ until very high couplings, at which the magnetic component becomes irrelevant.
We now look at $(1, 1)_S$ and $N = 9$. At very low couplings we still find a dispersion relation symmetric for $H_v = 0$ but, contrary to the $(\frac{1}{2}, 1)_S$ representation, there is no degeneracy (see Fig.3.5(a)).

[1]The Hamiltonian is defined up to constants as explained in Sec.1

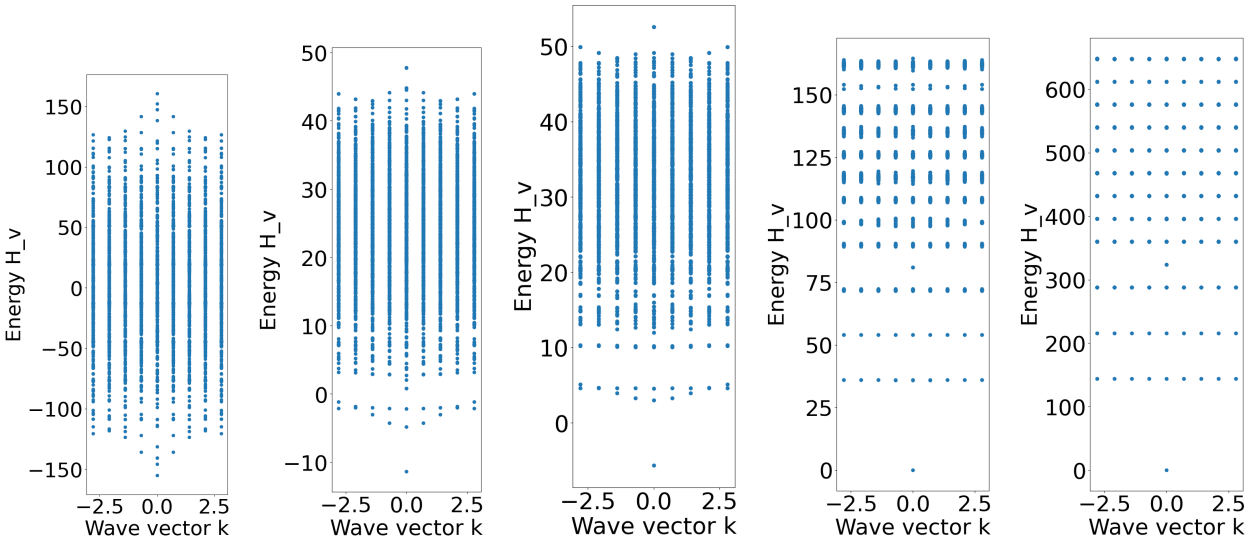

Figure 3.5: Every figure represents all the (k, H_v) couples at $N = 9$ and $(1, 1)_S$ for different values of the coupling: $g = 0.5$ (a), $g = 1.3$ (b), $g = 1.5$ (c), $g = 3$ (d) and $g = 6$ (e) .

However, we must bear in mind that for the $(\frac{1}{2}, 1)_S$ representation the horizontal links can not have zero value and this introduces an intrinsic degeneracy into the system. As the coupling grows, the lowest energy part of the dispersion relation separates itself from the rest (see Fig.3.5(b)). In contrast to the $(\frac{1}{2}, 1)_S$ representation, the lowest energy band is in fact composed of what seems to be two different bands mixed together. These two bands have approximately the same energy, but the slope and - therefore - the group velocity differ. This phenomenon could be explained by the breaking of the Lorentz symmetry due to the presence of the lattice. The nearly flat band could then be supported by longitudinal polarization (which is impossible in empty space where Lorentz symmetry is satisfied).
As the coupling continues to grow these two bands overlap and the rest of the dispersion relation separates itself into different bands (see Fig.3.5(d)). These bands are initially non-degenerate due to the magnetic component. But as the coupling grows, the magnetic contribution diminishes, thus resulting in complete degeneracy for very high couplings (see Fig.3.5(e)).
The GS remains separate and non-degenerate across all values of the coupling. The system shows an insulating behaviour only in the strong coupling regime, contrary to the $(\frac{1}{2}, 1)_S$ case. The low energy band remains clear and non-degenerate from $g \approx 1.2$ to $g \approx 2$.
We now take into consideration the low-energy region of the dispersion relation when it is clearly distinct from the bulk as seen in Fig.3.6. This distinction occurs only for certain values of the coupling. As previously stated, the bands in this region are always non-linear. Therefore, the group wave velocity is not constant.

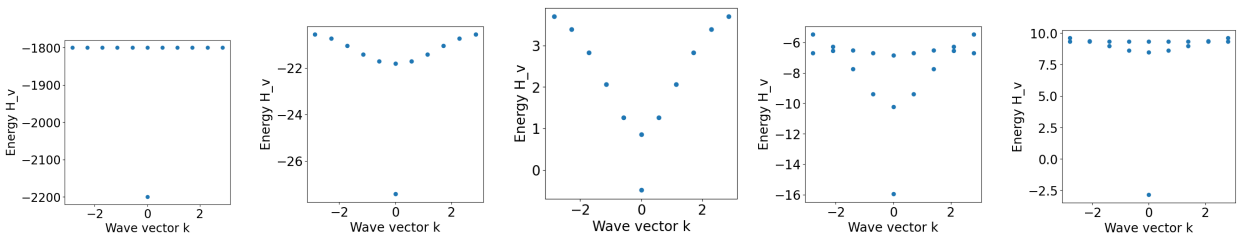

Figure 3.6: Pictures (a) to (c) show the low energy band for $N = 11$ and $(\frac{1}{2}, 1)_S$ at different couplings: $g = 0.1$ in (a), $g = 0.8$ in (b) and $g = 1.2$ in (c). Pictures (d) and (e) show the low energy bands for $N = 9$ and $(1, 1)_S$ at different couplings: $g = 1.2$ in (d) and $g = 1.7$ in (e).

This result is in contrast with what one would expect from electromagnetic wave propagation in empty space, namely a constant group velocity. Moreover, this result does not seem to change with the coupling or the spin representation, as the curvature of the band is present in all the cases analyzed. Increasing the size of the system would make the band clearer, but it is not doable with our computational means at the moment.

3.3 Wannier Functions

The Bloch States are defined in the reciprocal space. On the contrary, the Wannier Functions are obtained from the Bloch States and are defined in the real space as explained in 2.3.1. The main purpose of constructing WFs is to have spatially localized functions.
At first, we define the WFs using the simple formula in Eq.(2.8) which gives us non-symmetrized (NS) WFs as seen in Tab.3.1 and Tab.3.2. However, this definition is not the only possible one, as we can utilize the gauge freedom offered by the Bloch states. We can in fact replace every Bloch function in the n-band by

$$|\tilde{\Psi}_{nk}>= e^{\phi_n(k)}|\Psi_{nk}> \tag{3.1}$$

with $\phi_n(K)$ being a smooth periodical function in the reciprocal space. In our case, we can choose an arbitrary phase for each Bloch State. This would - in principle - allow us to localize the WFs. We could construct an operator that measures the localization of the WFs and then find the values of the phases that maximize the expectation value of said operator. Localized functions could then be used to construct wave packets and study their propagation across the system. However, this localization goes beyond the purposes of this study.
Instead, we exploit this gauge degree of freedom to construct symmetric WFs. The inversion operator $\hat{I}$ sends the Bloch states of the low energy band into the Bloch state of the same band with opposite wave vector eigenvalue with a phase θ.

$$R\Psi_{nk} = e^{i\theta}\Psi_{n(-k)} \tag{3.2}$$

$$R\Psi_{n(-k)} = e^{-i\theta}\Psi_{nk} \tag{3.3}$$

We then redefine the Bloch states adding the necessary phase in order to get the new inversion phase $\theta' = 2n\pi$.

$$\tilde{\Psi}_{nk} = e^{-\frac{\theta}{2}i}\Psi_{nk} \tag{3.4}$$

$$\Longrightarrow R\tilde{\Psi}_{nk} = e^{-\frac{\theta}{2}i}R\Psi_{nk} = e^{-\frac{\theta}{2}i}e^{\theta i}\Psi_{n(-k)} = e^{+\frac{\theta}{2}i}\Psi_{n(-k)} = \tilde{\Psi}_{n(-k)} \tag{3.5}$$

$$\tilde{\Psi}_{n(-k)} = e^{+\frac{\theta}{2}i}\Psi_{n(-k)} \tag{3.6}$$

$$\Longrightarrow R\tilde{\Psi}_{n(-k)} = e^{+\frac{\theta}{2}i}R\Psi_{n(-k)} = e^{+\frac{\theta}{2}i}e^{-\theta i}\Psi_{nk} = e^{-\frac{\theta}{2}i}\Psi_{nk} = \tilde{\Psi}_{nk} \tag{3.7}$$

If we now use these new Bloch States, the resulting WFs obtained from Eq.(2.8) are symmetric.
We now focus on the $(\frac{1}{2},1)_S$ case. Our formula is well-defined only if we utilize the Bloch States of a single energy band. In order to do this, we restrict our coupling values g to the ones which return a single definite low-energy band. As we can see from the graphs in Tab.3.1, the WFs exhibit different behaviors as N and g vary. Some WFs show a fairly clear localization (see Tab.3.1, $g = 0.5, N = 9, NS$), while other WFs seem to exhibit multiple localization points (see Tab.3.1, $g = 1.0, N = 11, NS$) or regions of uniform localization (see Tab.3.1, $g = 0.5, N = 11, NS$). If we look at the symmetrized WFs, there is no clear improvement. Sometimes the WFs become less localized (see Tab.3.1, $g = 0.5, N = 9$), but we never obtain well-localized functions. We also notice that the shape of the WFs remains constant when the value of the coupling remains inside a certain region (see Tab.3.1, $g = 1.0$ *to* $g = 1, 2, N = 9$).

We now shift our focus to $(1,1)_S$. In this case, we always have what seems to be two distinct low-energy bands mixed together, as explained in 3.2. As a first approximation, we take only the lowest energy states across the Brillouin Zone to construct our WFs. We deem this approximation sufficient for the purposes of our study. However, properly constructing the WFs would require a more

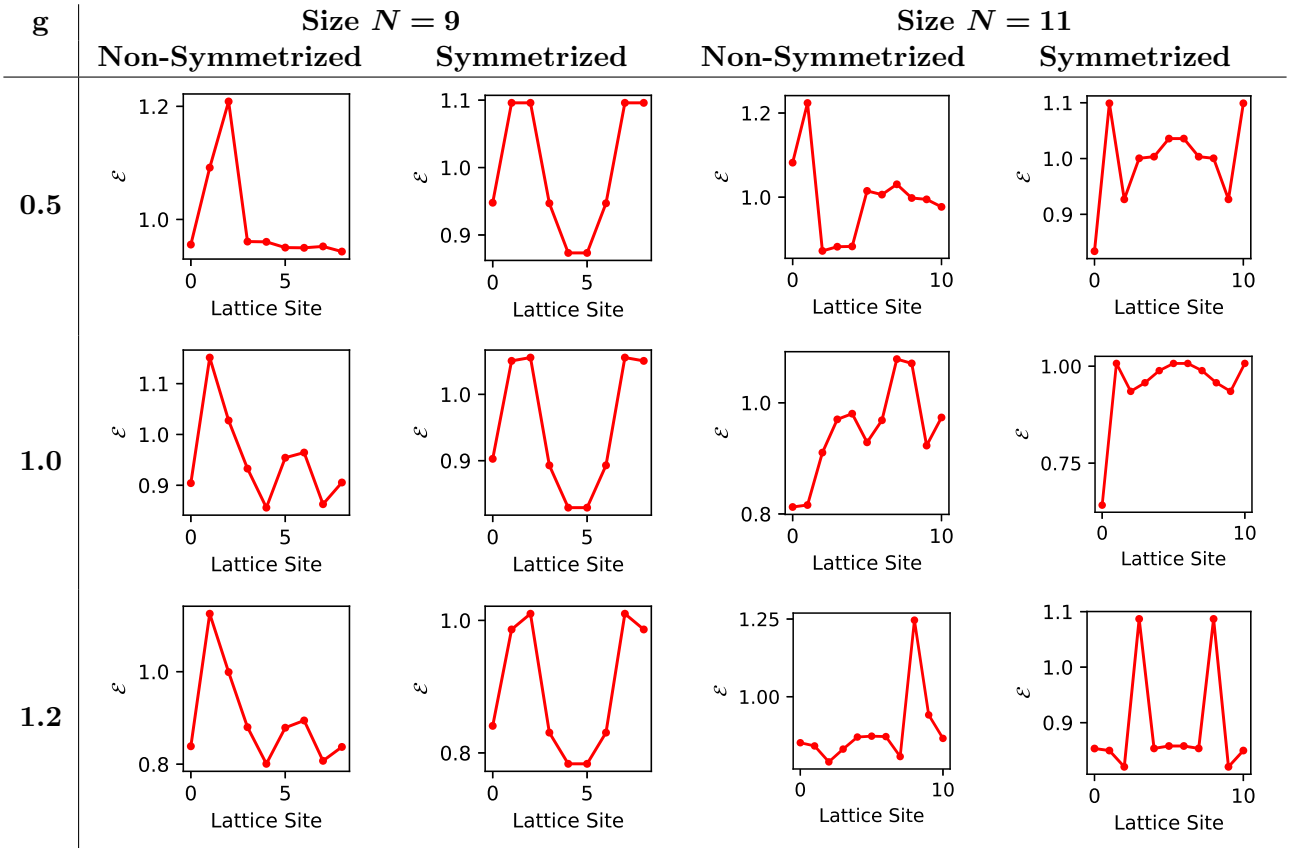

Table 3.1: The graphs refer to $(\frac{1}{2}, 1)_S$ and show the value of the "localization operator" (Eq.(2.9)) on the y-axis for the different values of r_x on the x-axis, thus giving an intuitive idea of the localization of a Wannier Function.

accurate analysis of the low energy region of the dispersion relation. At any rate, the localization seems to improve compared to the $(\frac{1}{2}, 1)_S$ case, as we can see some very well localized WFs (see Tab.3.2, $g = 1.3, 1.4, N = 7, NS$). However, some WFs remain non-localized (see Tab.3.2, $g = 1.3, N = 9, S$). The symmetrization procedure continues to give inconsistent results: sometimes it keeps the "localization" approximately constant (see Tab.3.2, $g = 1.4, N = 7$), sometimes it worsens it (see Tab.3.2, $g = 1.4, N = 9$).

The mixed results obtained from the symmetrization procedure were to be expected, as we did not take into account the localization of the function themselves.

3.4 Out of Equilibrium Dynamics

The object of our study is the response of our system to the $\hat{H}_A$ Hamiltonian (see Eq.(2.7)) with a step function as $\Omega(t)$:

$$\Omega(t) = c \cdot \Theta(t) \qquad (3.8) \qquad \Theta(t) = \begin{cases} 1 \ if \ t > 0 \\ 0 \ otherwise \end{cases} \qquad (3.9)$$

where c is called the "step height". We fix the spin representation to $(1, 1)_S$ and the coupling to $g = 1.5$, in order to have a definite low energy band as explained in 3.2. First of all, we need to find the right time step to make the RK4 algorithm converge. We analyze how the distance between vectors (see Eq.(2.20)) calculated at a fixed time t varies as we change the time step h and the step height c. We notice that if we fix c and the time steps h_1, h_2 the distance between the vectors $d(|v1(c, h_1; t)\rangle, |v2(c, h_2; t)\rangle = d(t)$ grows with time (see Fig.3.7). This result is to be expected, as we are repeating approximate calculations in a recursive way and therefore the errors we introduce at each step propagate in the following steps. We also notice that the distance grows more rapidly for

g	Size $N = 7$ Non-Symmetrized	Size $N = 7$ Symmetrized	Size $N = 9$ Non-Symmetrized	Size $N = 9$ Symmetrized
1.3	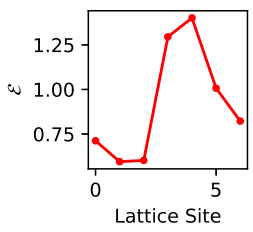	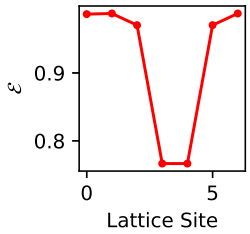	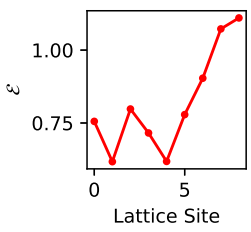	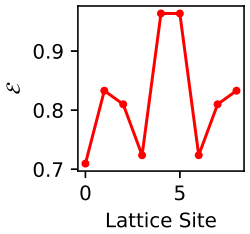
1.4	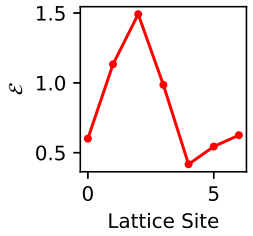	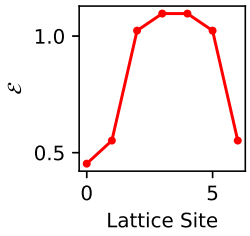	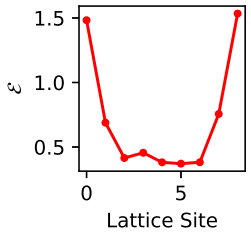	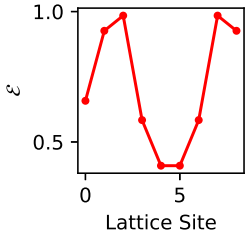

Table 3.2: The graphs refer to $(1,1)_S$ and show the value of the "localization operator" (Eq.(2.9)) on the y-axis for the different values of r_x on the x-axis, thus giving an intuitive idea of the localization of a Wannier Function.

higher values of c. Higher values of c induce faster waves and therefore a smaller step is needed to capture the evolution of the vector with the same precision as in the lower c cases.

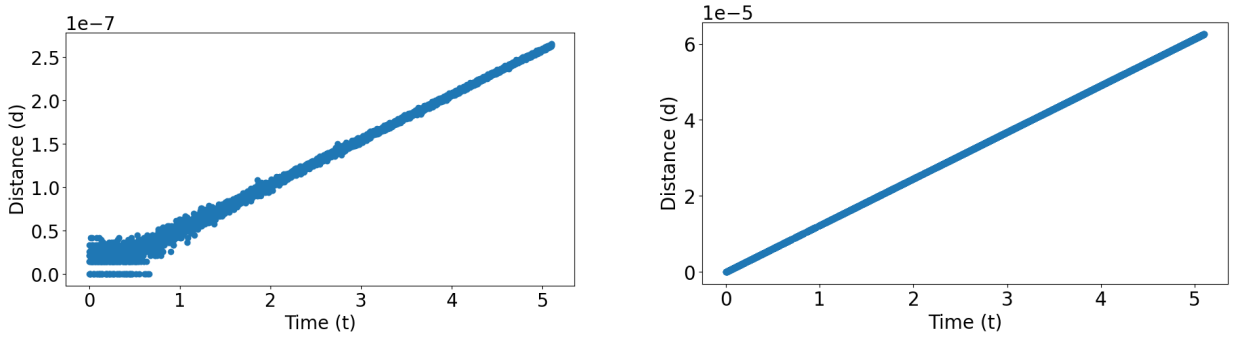

(a) (b)

Figure 3.7: These graphs represent how the distance (y-axis) between the vectors obtained from two different time steps at c fixed varies with time (x-axis).
(a) shows the graph for $c = 10$ and $h_1 = 0.0002, h_2 = 0.0005$
(b) shows the graph for $c = 30$ and $h_1 = 0.0002, h_2 = 0.0005$

Moreover, we look at distance as a function of the time step h for t, c fixed $d(|v1(c,t;h)\rangle, |v2(c,t;h)\rangle = d(h)$. The distance grows monotonically with h, but we can distinguish three different regimes:

- "low-h" region: there is a power law between h and d
- "intermediate-h" region: the distance grows increasingly faster with h until it reaches $d = 1$
- "high-g" region: the distance saturates at $d = 1$

This induces us to think that the RK4 algorithm converges in the "low-h" region. In this region the evolving vector is in fact stable: if the algorithm had not reached the convergence, we would have expected the vector to evolve chaotically, and therefore we would expect a significant increase in the

distance as the time step grows.

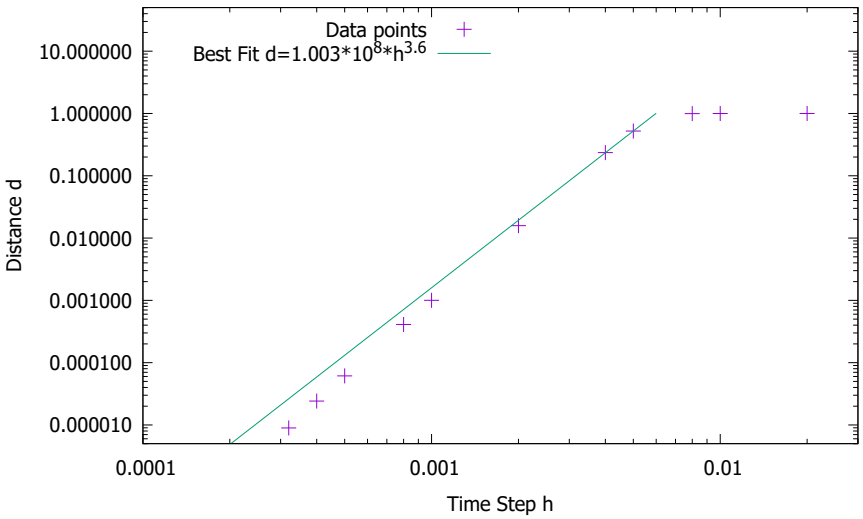

Figure 3.8: This graph shows the distance (y-axis) between the vector obtained for $t = 5, h = 0.0005$ and the vector obtained for $t = 5, h = 0.0002$ for $c = 30$

A time-step of $h = 0.0002$ is sufficient to reach the convergence in $t \in [0, 5]$ for $c = 30$. Since the distance can only diminish for lower values of t and c, a time step $h = 0.0002$ is sufficient for our purposes.
We now look at how the system evolves for different values of c. To represent the evolution of the system we show how the expectation values of the energy density operators defined in equations Eq.(2.9) and Eq.(2.21) evolve in time. This gives us an intuitive understanding of how the excitations propagate in the system. The oscillations of the energy density operators in the different sites are on very different scales: the intensity of the oscillations decreases rapidly as the distance from the starting plaquette grows. Moreover, the oscillations are both positive and negative and therefore the log scale is not a viable solution. Therefore, we need a rescaling that allows us to represent positive and negative values with continuity at $y = 0$ across different orders of magnitude. We choose the following: we first subtract the expectation value of the plaquette (for $\mathcal{B}$) or link (for $\mathcal{E}$) at $t = 0$ (which is the expectation value of the GS) and then we rescale our values (called y in the following equation) by using the following function:

$$y' = sgn(y) \log(1 + |y| \cdot 10^4) \tag{3.10}$$

This rescaling allows us to show very clearly even small oscillations of the expectation values from the original expectation value of the GS. If we look at Tab3.3 the first thing to notice is that the intensity of the oscillations always diminishes as the distance from the starting plaquette grows. This effect is to be expected, considering $\hat{H}_A$ acts on the first plaquette. If we now look at the electric field, we notice that the frequency of the oscillations of the first and second link grows monotonically with c. This phenomenon is caused by the growth of the energy - which grows monotonically with c - associated with the induced waves: this growth induces an increase in the frequency. It is difficult to obtain a group velocity for the propagating waves from these graphs, as we do not observe ballistic wave propagation through the system. The waves seem to exhibit a diffusive motion through the system, which may be caused by multi-band excitations.
However, if we only look at the first plaquettes (or links) it is possible to extract an approximate estimate of the propagation velocity across the first sites. We estimate the velocity for $c = 10$ and $N = 5$. The result is of the same order of magnitude as the maximum group velocity (see Eq.(2.22))obtained from the analysis of the energy bands. We use the temporal position of the maximums of the excitations on the different plaquettes or links as an estimate of the group velocity derived from the OOE

dynamics. The chosen maximums for this estimation are shown in Fig.3.9. We then calculate the average time interval it takes for an excitation to propagate between two links or plaquettes. We call $t_i^E(j)$ the time of the j-th maximum of $\mathcal{E}$ on the i-th link and $t_i^B(j)$ the time of the j-th maximum of $\mathcal{B}$ on the i-th plaquette. If we consider P maximums, the average time interval and the associated velocity from the i-th to the $i+1$-th link or plaquette are:

$$\bar{t}(i \to i+1) = \sum_{j=1}^{P} \frac{t_{i+1}(j) - t_i(j)}{P} \tag{3.11}$$

$$v(i \to i+1) = 1/\bar{t}(i \to i+1) \tag{3.12}$$

	Electric Field	Magnetic Field
c=5	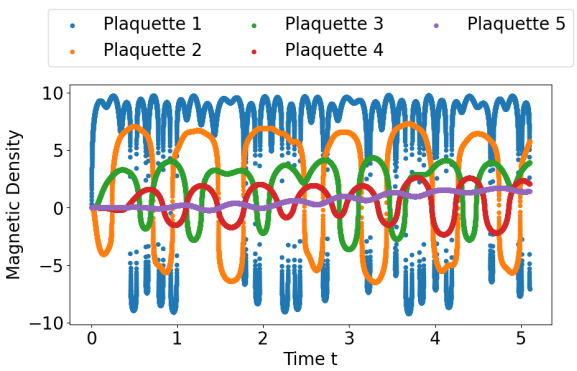	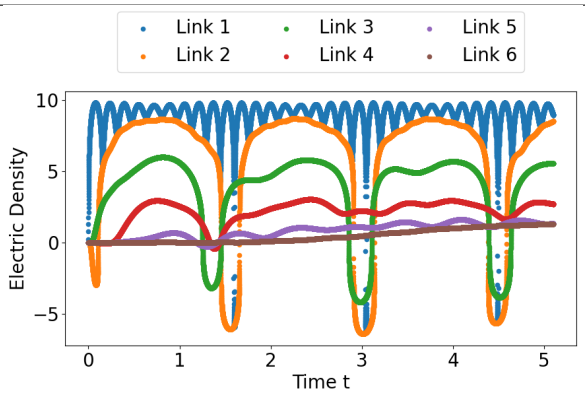
c=15	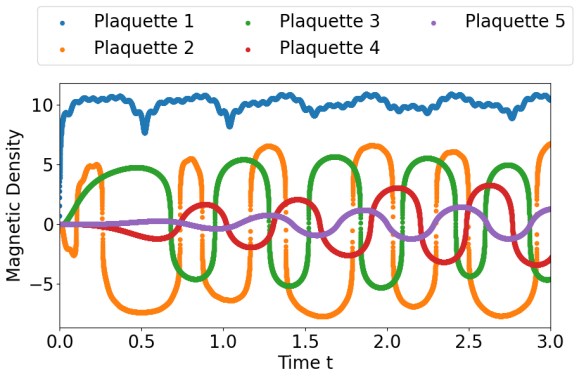	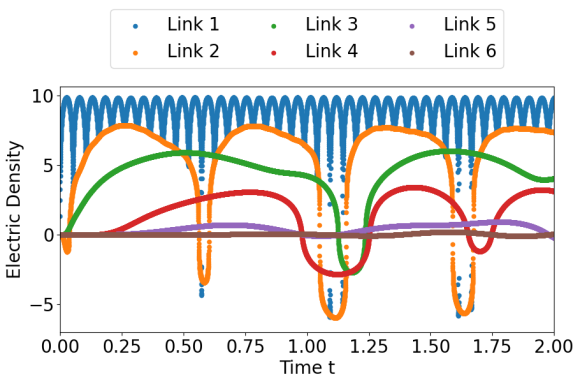
c=25	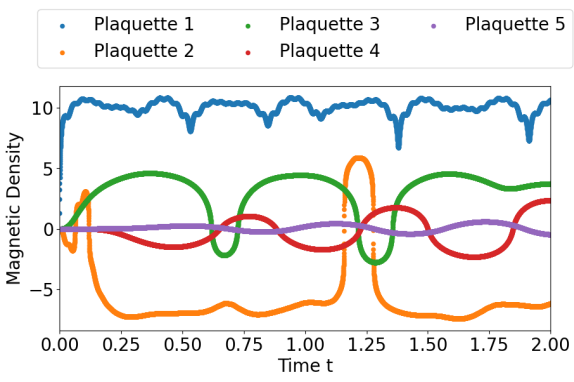	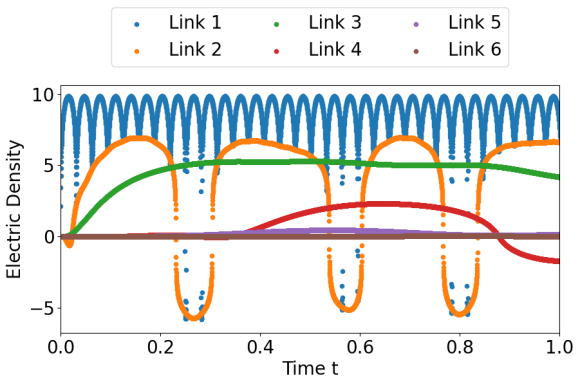

Table 3.3: These graphs show the oscillations of the energy density expectation values (y-axis) (compared to the GS expectation value) as a function of time (x-axis).

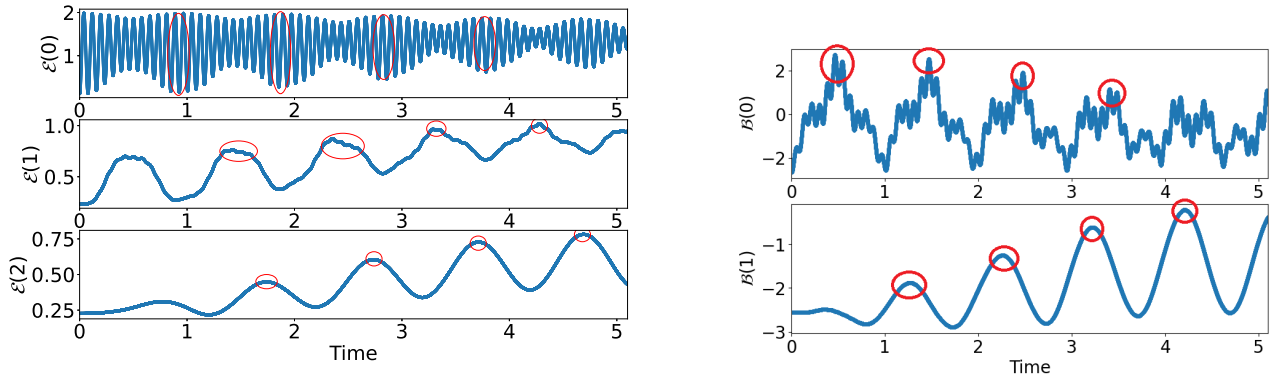

(a) (b)

Figure 3.9: These graphs refer to the $N = 5, g = 1.5, c = 10$ case and show how the expectation values of the $\mathcal{E}, \mathcal{B}$ operators (y-axis) evolve in time (x-axis). The central parts of the regions circled in red are taken as a time reference to estimate the propagation velocity of the excitations.
(a) shows the expectation value of $\mathcal{E}$ for the first ($\mathcal{E}(0)$), second ($\mathcal{E}(1)$), and third ($\mathcal{E}(2)$) vertical links
(b) shows the expectation value of $\mathcal{E}$ for the first ($\mathcal{B}(0)$) and second ($\mathcal{B}(1)$) plaquette

We show some examples of $v(i \to i+1)$ and $\ddot{v}_g$ in Fig.3.10. The estimated velocities range from $v \approx 1$ to $v \approx 3$, while $\ddot{v}_g \approx 1.83$ for the green band and $\ddot{v}_g \approx 0.64$ for the red band. The order of magnitude of the OOE estimations is the same as the order of magnitude of the values obtained from the equilibrium analysis, as expected. However, the values seem to suggest that with these intensities of $\hat{H}_A$ we are in fact exciting the green band. The number of oscillations in the first link in Fig.3.9 suggests trying $c \approx 1$, however for these values of c the induced oscillations are smaller. In fact, we have yet to pinpoint the right value of c to excite oscillations in the lowest energy band. Further research on how the "quantity of oscillations" varies for different values of c should be able to give us a better understanding of the system dynamics when excited.

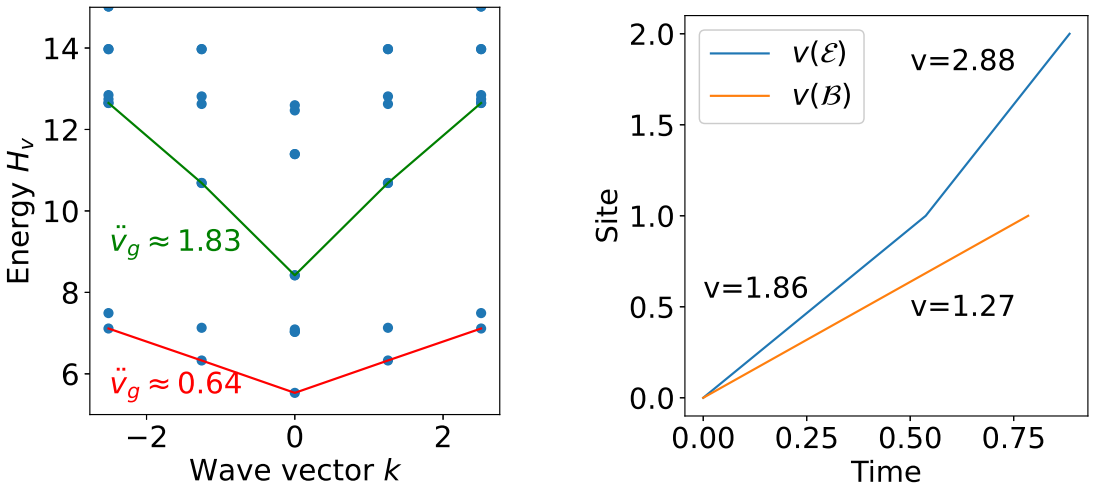

(a) (b)

Figure 3.10: These graphs compare the maximum group velocity of two low energy bands for $N = 5, g = 1.5$ to the estimate of the propagation velocity extracted from the analysis of the OOE oscillations in Fig.3.9.
(a) shows two distinct low energy bands, $\ddot{v}_g \approx 1.83$ for the green band and $\ddot{v}_g \approx 0.64$ for the red band.
(b) shows the estimated propagation velocities for the OOE dynamics, the site number refers to the link number for $\mathcal{E}$ and the plaquette number for $\mathcal{B}$

Chapter 4

Conclusion

Simulating real-time dynamics of gauge theories with matter particles is challenging. In this sense, Hamiltonian lattice gauge theories give us a practical toolbox to perform numerical calculations of high-energy systems and processes in the practical formalism of quantum many-body lattice theories. Obtaining analytical solutions is virtually impossible without making some approximations, and even then only small system sizes are solvable from a computational point of view. However, these simple systems are still able to give us an insight into the complex interplay between the forces at work.
First of all, the systems with periodic boundary conditions display some obvious symmetries under reflection and translation, which show unequivocally the invariance of the Hamiltonian under these operations. When looking at the single configurations it is possible to see the effects of the electric and magnetic terms separately. Each of them introduces a clear order among the configurations energy-wise. The interplay between the two terms eliminates the degeneracy at intermediate couplings. Moreover, in this regime there is a clear non-degenerate low energy band, which could - in principle - support the propagation of waves. In contrast to the classical case, the dispersion relation is not linear, but we must bear in mind that we restricted ourselves to small system sizes and low spin representations. We expect to retrieve the classical limit for bigger sizes and representations. The Wannier functions are not very well localized. This result was to be expected as we do not properly address the gauge degree of freedom inherently present in the definition of the Bloch States. The out-of-equilibrium dynamics analysis is still in the early stages. We know how to evolve our states under the action of the time-dependent Hamiltonian, but we still have not found the right modes of excitation for the system.
Further research is needed to better understand if this framework, namely Hamiltonian Lattice Gauge Theories and Quantum Link Models, is sufficient to study more complex phenomenons, like the Compton effect and the Bragg Scattering. In particular, we would like to study the localization of the Wannier Functions and to better understand the propagation of waves in the out-of-equilibrium case. Localizing the Wannier Functions would allow us to construct wave packets which we could then send into the system. The propagation of waves is interesting in itself as a way to understand how to excite a specific energy band of the system. We expect to find ballistic wave propagation with the group velocity of the band when exciting the system with the right modes. After these analyses we could then introduce the added complexity of a non-zero fermionic matter field, thus being able to study the more complex phenomenons mentioned above.

List of Figures

List of Tables

Bibliography

[1] S. Chandrasekharan D. Chen A. Tsapalis B. Beard, R. Brower and U.J. Wiese. D-theory: field theory via dimensional reduction of discrete variables. *Nuclear Physics B - Proceeding Supplements*, 63:775.

[2] C.D.T.Runge. *Mathematische Annalen*, 46:167–178, 1895.

[3] S. Chandrasekharan and U. J. Wiese. Quantum link models: A discrete approach to gauge theories. *Nuc. Phys. B*, 492:355–471, 1997.

[4] M. Creutz. *Quarks, gluons and lattices*. Cambridge University Press, 1997.

[5] T. DeGrand and C. DeTar. *Lattice Methods for Quantum Chromodynamics*. World Scientific, 2006.

[6] C. Gattringer and C. B. Lang. *Quantum Chromodynamics on the lattice*. Springer-Verlag, 2010.

[7] D. Horn. Finite matrix models with continuous local gauge invariance. *Physics Letters B*, 100: 149, 1981.

[8] J. Kogut. An introduction to lattice gauge theory and spin systems. *Rev. Mod. Phys.*, 51:659, 1979.

[9] J. Kogut and L. Susskind. Hamiltonian formulation of wilson's lattice gauge theories. *Phys. Rev. D*, 11:395, 1975.

[10] Elliot H. Lieb and Derek W. Robinson. *Communications in Mathematical Physics*, 28:251–257, 1972.

[11] I. MOntvay and G. Muenster. *Quantum Fields on a lattice*. Cambridge University Press, 1994.

[12] M.W.Kutta. *Zeitschrift für Mathematik und Physik*, 46:435–453, 1901.

[13] P. Orland and D. Rohrlich. Lattice gauge magnets: Local isospin from spin. *Nuclear Physics B*, 338:647, 1990.

[14] S. Chandrasekharan R. Brower and U. J. Wiese. Qcd as a quantum link model. *Phys. Rev. D*, 60:094502.

[15] K. G. Wilson. Confinement of quarks. *Phys. Rev. D*, 10:2445, 1974.